

Cosmic microwave background: polarization and temperature anisotropies from symmetric structures

Carlo Baccigalupi

SISSA/ISAS, Via Beirut 4 34014 Trieste, Italy

Perturbations in the Cosmic Microwave Background (CMB) are generated by primordial inhomogeneities. I consider the case of CMB anisotropies from one single ordered perturbation source, or seed, existing well before decoupling between matter and radiation. Such structures could have been left by high energy symmetries breaking in the early universe.

I focus on the cases of spherical and cylindrical symmetry of the seed. I give general analytic expressions for the polarization and temperature linear perturbations, factoring out of the Fourier integral the dependence on the photon propagation direction and on the geometric coordinates describing the seed. I show how the CMB perturbations manifestly reflect the symmetries of their seeds. In particular, polarization is uniquely linked to the shape of the source because of its tensorial nature.

CMB anisotropies are obtained with a line of sight integration. They are function of the position and orientation of the seed along the photons path.

This treatment highlights the undulatory properties of the CMB. I show with numerical examples how the polarization and temperature perturbations propagate beyond the size of their seeds, reaching the CMB sound horizon at the time considered. Just like the waves from a pebble thrown in a pond, CMB anisotropy from a seed intersecting the last scattering surface appears as a series of temperature and polarization waves surrounding the seed, extending on the scale of the CMB sound horizon at decoupling, roughly 1° in the sky. Each wave is characterized by its own value of the CMB perturbation, with the same mean amplitude of the signal coming from the seed interior; as expected for a linear structure with size $L \leq H^{-1}$ and density contrast δ at decoupling, the temperature anisotropy is $\delta T/T \simeq \delta(L/H^{-1})^2$, roughly ten times stronger than the polarization.

These waves could allow to distinguish relics from high energy processes of the early universe from point-like astrophysical sources, because of their angular extension and amplitude. Also, the marked analogy between polarization and temperature signals offers cross correlation possibilities for the future detection instruments. It would be interesting to detect these signals in the next $10'$ CMB map provided by the Planck Surveyor satellite experiment.

PACS: 98.70.Vc 98.80.Cq

FERMILAB-Pub-98/204-A

I. INTRODUCTION

The cosmic microwave background (CMB) carries detailed information about the high energy physical processes occurred in the early universe. Most probably, the microphysics still hidden to our knowledge left traces that have been stretched out to large and observable scales by a period of accelerated expansion; at decoupling between matter and radiation, they imprinted anisotropies in the CMB. This is the reason of the contemporary theoretical and experimental efforts to understand the CMB physics. The theory of the CMB anisotropies has been deeply explored in the past (see [2,13] and references therein) and, recently, it has been casted in a complete and organic form [7]. At the same time, many experiments are at work to explore the CMB anisotropies toward smaller and smaller angular scales (see [12] for reviews); this experimental enterprise will culminate with the Planck mission of the next decade, that will provide the whole sky temperature and polarization anisotropy map down to a minimum detectable perturbation of one part over 1 million and with an angular resolution of about $10'$ [15].

According to the inflationary phenomenology, a scalar field (the inflaton) slowly rolls toward the minimum of its potential, giving the non-zero vacuum energy responsible for the expansion itself. The quantum fluctuations are thought to arise from the vacuum in a curved background; they are stretched out to large scales by the inflationary expansion itself, and set up the seeds of the cosmological perturbations we observe today (see [11] for reviews). However, even adopting this inflationary scenario, things are still unclear for what concerns the release of the energy stored in the inflaton into ordinary matter and radiation, the so called reheating (or *preheating*) era [8]. The oscillations of the inflaton around its minimum, combined with the coupling to other fields, can restore high energy symmetries that have to be broken to reach our low energy minimum; consequently, a post-inflationary generation of topological defects may arise, and this occurrence is at the present under investigation [16]. Also, during inflation itself many fundamental fields may act on stage and the effective potential may have several minima separated by potential barriers. If this is the case, tunneling phenomena occur, and the nucleated bubbles are stretched out to large scales as the ordinary quantum fluctuations (see [4] for reviews); at reheating the energy stored in the shells is converted into matter and radiation and bubbly traces may be left in the density distribution (this possibility, with different points of view, has been considered in the last decade [9]).

Suppose that one of these relics from very high energy physics is plunged from some very early time into cosmic matter and radiation, no matter of its composition, that could be scalar field or cosmic fluid or other. It generates perturbations around itself, in particular in the photon-baryon fluid. If also it intersects the last scattering surface (LSS, the place of origin of the CMB), these perturbations become anisotropies that we could observe today. These are expected to be well recognizable, since in most cases such seed is a spatially limited structure, very different from the diffuse fluctuations of the pure slow-roll inflation; technically speaking, such signal would be strongly non-Gaussian and non-scale-invariant. Also, such structures are expected to possess (approximate) symmetries, like a bubble or a monopole (spherical) and a string (cylindrical). Their detection in the CMB anisotropies would be the first observational evidence of the existence of high energy symmetries, and this hope is precisely the motive of this work. I develop here some useful formulas for the CMB perturbations and anisotropies from symmetric structures; the results are *independent* from the particular seed, the only characterization being its symmetry, that I take here spherical or cylindrical. I perform some numerical integrations using these formulas and adopting toy symmetric seeds, in order to investigate the geometrical and dynamical properties of their own CMB perturbations and anisotropies. In forthcoming works I will compute the CMB anisotropies from realistic relics left from high energy physics in the early universe; a pretty example, valid simply for large bubbles in the density distribution, may be found in [1].

As already mentioned, the treatment of the CMB inhomogeneities has been casted recently in a complete and organic form, the total angular momentum method [7]. In turn, it is based on the general treatment of the linear cosmological perturbations [2]; I perform the calculations in this frame, respecting the notations as much as possible. The CMB perturbations involve temperature ($\delta T/T \equiv \Theta$ in the following) and polarization, that is expressed via the Stokes parameters Q and U describing linear polarization. For a given Fourier mode specified by the \vec{k} vector, it is convenient to express the relevant quantities in a frame in which the \hat{k} direction is the polar axis (the \hat{k} -frame in the following). The reason is that, in the new frame, the scalar, vector and tensor components of the perturbed metric quantities are coupled respectively to the $m = 0, \pm 1, \pm 2$ indexes of the spherical harmonics [7]. Of course, transforming back to the real space, the \hat{k} -frame quantities must be expressed in the fixed laboratory frame (the *lab*-frame in the following). For a given Fourier mode \vec{k} , Q is the difference in temperature fluctuations polarized in the \hat{e}_θ and \hat{e}_ϕ directions (θ and ϕ being the usual angles in spherical coordinates); U is the same difference where the axes have been rotated by 45° around the photon propagation direction. Equivalently, Q and U may be seen as the expansion coefficients of the polarization tensor into the Pauli matrices σ_3 and σ_1 , defined on the basis vectors \hat{e}_θ and \hat{e}_ϕ in the \hat{k} -frame.

The background Friedmann Robertson Walker (FRW) metric is

$$ds^2 = a(\eta)^2 \left(-d\eta^2 + \frac{dr^2}{1 - Kr^2} + r^2 d\Omega^2 \right), \quad (1)$$

where $\eta(t) = \int_0^t d\tau/a(\tau)$ is the conformal time and K the spatial curvature; I will assume a flat $K = 0$ background in this work. The perturbed metric tensor is

$$g_{\mu\nu} = a(\eta)^2 (\gamma_{\mu\nu} + h_{\mu\nu}), \quad (2)$$

where $a(\eta)^2 \gamma_{\mu\nu}$ represents the background. Since $h_{\mu\nu} \ll \gamma_{\mu\nu}$, a gauge freedom reduces the number of physically significant quantities in the perturbation metric tensor; in this work I adopt the generalized Newtonian gauge in which the two scalar perturbed metric component are $\Psi = h_{00}/2$ and $2\Phi = h_{11} = h_{22} = h_{33}$ [2,7].

The CMB perturbations depend on the spacetime point and on the photon propagation direction \hat{n} , so an appropriate normal mode expansion is needed:

$$\Theta(\eta, \vec{r}, \hat{n}) = \int \frac{d^3k}{(2\pi)^3} \sum_l \sum_{m=-2}^2 \Theta_l^{(m)}(\eta, \vec{k}) G_l^m(\vec{r}, \vec{k}, \hat{n}), \quad (3)$$

$$(Q + iU)(\eta, \vec{r}, \hat{n}) \mathbf{M}_+ + (Q - iU)(\eta, \vec{r}, \hat{n}) \mathbf{M}_- =$$

$$\int \frac{d^3k}{(2\pi)^3} \sum_{l \geq 2} \sum_{m=-2}^2 \left[(E_l^{(m)} + iB_l^{(m)})(\eta, \vec{k})_{+2} G_l^m(\vec{r}, \vec{k}, \hat{n}) + (E_l^{(m)} - iB_l^{(m)})(\eta, \vec{k})_{-2} G_l^m(\vec{r}, \vec{k}, \hat{n}) \right], \quad (4)$$

where $\mathbf{M}_\pm = (\sigma_3 \mp i\sigma_1)/2$ are convenient basis matrices for the polarization tensor. G_l^m and ${}_{\pm 2}G_l^m$ include both spatial and angular functions; the spatial ones are the eigenmodes of the Laplacian in the metric (1):

$$\nabla^2 Q_K(\vec{k}, \vec{x}) \equiv \gamma^{ij} Q_{K|ij} = -k^2 Q_K(\vec{k}, \vec{x}); \quad (5)$$

the angular functions are instead spherical harmonics. In the case of flatness ($K = 0$) the Laplace equation (5) gives plane waves, and the expression of the normal modes becomes

$$G_l^m = (-i)^l \sqrt{\frac{4\pi}{2l+1}} Y_l^m(\hat{n}_{\vec{k}}) \exp(i\vec{k} \cdot \vec{r}) , \quad (6)$$

$$\pm_2 G_l^m = (-i)^l \sqrt{\frac{4\pi}{2l+1}} \pm_2 Y_l^m(\hat{n}_{\vec{k}}) \mathbf{M}_{\pm}^{\hat{k}} \exp(i\vec{k} \cdot \vec{r}) ; \quad (7)$$

as a difference with respect to [7], the notation $\hat{n}_{\vec{k}}$, $\mathbf{M}_{\pm}^{\hat{k}}$ has been used to underline that, for each \vec{k} mode, all the quantities in (6,7), as well as the expansion coefficients in (3,4), are expressed in the \hat{k} -frame; as customary, the expansion coefficients of the Stokes parameters Q, U have been decomposed into real and imaginary parts. Throughout this work, in order to characterize the polarization within symmetric seeds, I make use of the useful definition of *polarization direction* [3], given entirely in terms of Q and U as follows. It is easy to see that, due to the rotation properties of the Pauli matrices, the angle

$$\alpha = \frac{1}{2} \tan^{-1} \frac{U}{Q} \quad (8)$$

goes into $\alpha - \phi$ under a rotation by ϕ around \hat{n} ; thus it defines a fixed axis on the plane orthogonal \hat{n} , that is the polarization direction.

The underlying cosmological inhomogeneities move the CMB perturbations and are encoded in the expansion coefficients in (3,4). Before going to the content of this work, it is useful to point out the following important distinction. The Fourier transform of any perturbation quantity Δ may be written as

$$\Delta(\vec{k}) = |\Delta(\vec{k})| e^{i\phi_{\vec{k}}} ; \quad (9)$$

it is Gaussian if the phases in $\phi_{\vec{k}}$ are random; specifically in these hypothesis, the statistics is completely described by the power spectrum, $\langle |\Delta(\vec{k})|^2 \rangle$. Also it is scale-invariant if the modulus depends only on the scale ($k = |\vec{k}|$) in such a way that the power associated to each one is the same at the horizon reenter. On the contrary, CMB anisotropies from sources like the ones considered here are non-Gaussian and non-scale-invariant; their symmetries, encoded in precise properties of both modulus and phases in (9), are their unique sign in the CMB. Moreover, I do not require that they are dominant for structure formation. An high resolution CMB map could contain the unambiguous imprint of one single symmetric seed existing at decoupling plunged in a global Gaussian signal; even if the power spectrum does not contain its sign at all, that would be enormously interesting!

The work is organized as follows. Sections II and III contain the analysis of the CMB perturbations in spherical and cylindrical symmetry respectively. Section IV contains the method for the computation of the CMB polarization and temperature anisotropies as they would appear on the sky. In section V the results from numerical integrations are shown. Finally, section VI contains the conclusions.

II. SPHERICAL SYMMETRY

It is easy to see that spherical structures may be scalar only, and thus are described by the $m = 0$ modes of the linear expansion; there is no way to comb the hair of a sphere in such a way to obtain a spherical distribution, and this prevents spherical structures to be made of genuinely vector (or tensor) components. Thus I drop the (0) index in the following, and consider flat space geometry, $K = 0$.

The problem to solve is the following: at a conformal time η , a perfect CMB detector is placed in a point \vec{r} nearby a primordial spherical structure; what's the CMB perturbations carried by photons scattered on a direction \hat{n} ?

The center of the coordinate frame is placed at the center of the spherical seed. Its Fourier transform depends only on the wavevector modulus k and it is therefore the same for any axes orientation:

$$\vec{r} \rightarrow r \Leftrightarrow \vec{k} \rightarrow k . \quad (10)$$

First, let us find the consequence of (10) on the pure temperature perturbation Θ . The expansion coefficients Θ_l in (3) are proportional to the Fourier transformed perturbation (see section V) and do not depend at all on the orientation of the perturbation in the \hat{k} -frame, simply because it is spherical: they depend on k only. Consequently, posing $d^3k = k^2 dk d\Omega_{\hat{k}}$ in (3) the Θ_l coefficients may be extracted from the angular integral. Thus let us face the pure geometric quantity

$$\int d\Omega_{\hat{k}} (-i)^l \sqrt{\frac{4\pi}{2l+1}} Y_l^0(\hat{n} \cdot \hat{k}) \exp(i\vec{k} \cdot \vec{r}) , \quad (11)$$

where the argument of the spherical harmonics in (6) has been shown (see appendix A). The integral (11) is easily computed expanding the plane wave into Bessel and Legendre functions

$$e^{i\vec{k}\cdot\vec{r}} = \sum_l i^l (2l+1) j_l(kr) P_l(\hat{r}\cdot\hat{k}), \quad (12)$$

and employing the useful relation (A11) with $\hat{n}_1 = \hat{k}$, $\hat{n}_2 = \hat{r}$ and $\hat{n}_3 = \hat{n}$. The result is:

$$\Theta = \sum_l P_l(\hat{n}\cdot\hat{r}) \int \frac{k^2 dk}{2\pi^2} \Theta_l(\eta, k) j_l(kr). \quad (13)$$

This expression gives the CMB temperature perturbation at any time for the most general spherical perturbation, encoded in the Fourier integral. The dependence on \hat{n} and \hat{r} has been factored out, and enters only in the Legendre polynomials argument $\hat{n}\cdot\hat{r}$. This is an expected feature of this spherical case: for example, focus on the $l=1$ term, better known as the Doppler effect (Θ_1 is essentially the velocity of baryons [13]); the motion of each particle in this spherical case is radial of course; then, since this Legendre polynomial is just $\hat{n}\cdot\hat{r}$, photons propagating on the direction \hat{n} pick up the usual Doppler cosine contribution at the scattering point.

Let us face now the polarization for a spherical seed. A first simplification is that the scalar perturbations excite the E_l modes only [7], so we can drop the B_l terms in the following. Then, as before, the E_l coefficients depend on k only, so they can be extracted from the angular integral. As a difference from the temperature case, the *tensor* spherical harmonics describe now the angular dependence in (7); fortunately they admit, for $m=0$, a simple expression in terms of the elementary Legendre polynomials, as it is demonstrated in appendix A:

$${}_2Y_l^0(\hat{n}\cdot\hat{k}) = \sqrt{\frac{2l+1}{4\pi} \frac{(l-2)!}{(l+2)!}} P_l^2(\hat{n}\cdot\hat{k}), \quad (14)$$

where the \pm index has been suppressed since it makes no difference in the $m=0$ case.

Focus now on the $\mathbf{M}_{\pm}^{\hat{k}}$ matrices. They have to be expressed in terms of the fixed *lab*-frame matrices \mathbf{M}_{\pm} . This is obtained performing a rotation around the \hat{n} axis in order to make the \hat{e}_{ϕ} and the \hat{e}_{ϕ} vectors in the \hat{k} -frame coincident with the laboratory ones: the rotation angle is essentially the angular coordinate of the projection of \hat{k} into the plane orthogonal to \hat{n} . For simplicity, but without any loss of generality, let's orient the *lab*-frame so that \hat{n} is the polar axis; then, it is easy to see that the rotation angle is simply $-(\phi_{\hat{k}} + \pi)$, where $\phi_{\hat{k}}$ is just the ϕ coordinate of \hat{k} in the *lab*-frame; thus, from elementary rotation properties of the Pauli matrices, the expression of $\mathbf{M}_{\pm}^{\hat{k}}$ as seen in the *lab*-frame is

$$\mathbf{M}_{\pm}^{\hat{k}} = e^{\mp 2i\phi_{\hat{k}}} \mathbf{M}_{\pm}. \quad (15)$$

The integral in (4) has now the following form:

$$(Q \pm iU) \mathbf{M}_{\pm} = \sum_{l \geq 2} \int \frac{k^2 dk}{(2\pi)^3} E_l(\eta, k) (-i)^l \sqrt{\frac{(l-2)!}{(l+2)!}} \int d\Omega_{\hat{k}} e^{i\vec{k}\cdot\vec{r}} P_l^2(\hat{n}\cdot\hat{k}) \cdot e^{\mp 2i\phi_{\hat{k}}} \mathbf{M}_{\pm}. \quad (16)$$

Moreover, it is useful to employ the expansion (12) together with the addition relation (A10) with $\hat{n}_1 = \hat{r}$ and $\hat{n}_2 = \hat{k}$:

$$e^{i\vec{k}\cdot\vec{r}} = \sum_{l,m=-l}^l i^l 4\pi j_l(kr) Y_l^m(\hat{r}) Y_l^{m*}(\hat{k}). \quad (17)$$

The integral (16) in $d\phi_{\hat{k}}$ can now be calculated: the $e^{\mp 2i\phi_{\hat{k}}}$ phases in (15) select the $m = \mp 2$ terms respectively above; once this is done, the integral on $d\theta_{\hat{k}}$ is simple using the spherical harmonics orthogonality (A3); the final result is

$$(Q + iU) \mathbf{M}_+ + (Q - iU) \mathbf{M}_- = (e^{-2i\phi_{\hat{r}}} \mathbf{M}_+ + e^{2i\phi_{\hat{r}}} \mathbf{M}_-) \cdot \sum_{l \geq 2} \sqrt{\frac{(l-2)!}{(l+2)!}} P_l^2(\hat{n}\cdot\hat{r}) \cdot \int \frac{k^2 dk}{2\pi^2} E_l(\eta, k) j_l(kr), \quad (18)$$

where $\phi_{\hat{r}}$ is the angular coordinate of the projection of the \vec{r} vector on the plane orthogonal to \hat{n} . Let's check out the meanings of (18). Again the dependence on \hat{n} and \hat{r} has been completely extracted from the Fourier integral; really the matrices \mathbf{M}_{\pm} , basis for the polarization tensor, are outside the sum on l and multiply appropriate phases: this makes easy the following geometric consideration. If we choose the *lab*-axes so that $\phi_{\hat{r}} = 0$, the matrix in (18) is simply $\mathbf{M}_+ + \mathbf{M}_- = \sigma_3$ and the polarization quantities results in a pure Q term; thus (18) gives the difference in the

polarization amplitudes relative to the axes displayed in the upper panel of figure 1, one lying on the plane formed by the \hat{n} and \hat{r} directions and the other orthogonal to the same plane. With this axes orientation, the angle α in (8) is zero: this means that the polarization direction within a spherical seed lies on the plane formed by \hat{n} and \hat{r} , as sketched in figure 1. As a related important point, note the second order Legendre polynomial P_l^2 (the temperature case had P_l); it is meaningful since it guarantees that light propagating radially is not polarized ($P_l^2 \propto \sin^2 \theta P_l$): the radial propagation in spherical symmetry is an axial symmetric problem, so that no preferred direction exists for the polarization, since it belongs on the plane orthogonal to the symmetry axis.

These results, together with the temperature ones, completely characterize the CMB perturbation carried by photons moving in a spherical seed, independently from any other specification. The next section contains the same analysis developed here, but based on cylindrical seeds.

III. CYLINDRICAL SYMMETRY

Scalars can be arranged cylindrically of course, but also vectors (vorticity is a vectorial feature). Consequently, the $m = 0, \pm 1$ are allowed. In the vector case however, the generic \vec{k} mode of the Fourier transform is a vector of course; thus its orientation enters in the angular integrals of (3) and (4), that become strongly dependent on the particular seed considered. For this reason, again I restrict to the scalar case (dropping the (0) index), and employ flat FRW, $K = 0$.

The Fourier transform of a cylindrically symmetric quantity Δ may be expressed as

$$\Delta(\eta, \vec{k}) \equiv \Delta(\eta, k_+, k_z) , \quad (19)$$

where k_z, k_+ are the component of \vec{k} on the symmetry axis and on the equatorial plane respectively, $k_+^2 = k_x^2 + k_y^2$. If the seed is invariant under traslations along the symmetry axis (this case is mentioned as infinite cylindrical seed in the following), then the expression is

$$\Delta(\eta, \vec{k}) \equiv \Delta(\eta, k_+) \cdot 2\pi\delta(k_z) , \quad (20)$$

where $\delta(k_z)$ is the Dirac delta. Consequently, the expansion coefficients of (3) and (4) depend only on k_+, k_z in the first case and on k_+ in the second.

First, consider the temperature perturbation. In cylindrical coordinates $d^3k = k_+ dk_+ dk_z d\phi_{\hat{k}}$ and the Θ_l coefficients come out of the integral in $d\phi_{\hat{k}}$:

$$\Theta = \sum_l \int \frac{k_+ dk_+ dk_z}{(2\pi)^3} \Theta_l(\eta, k_+, k_z) \int d\phi_{\hat{k}} (-i)^l \sqrt{\frac{4\pi}{2l+1}} Y_l^0(\hat{k} \cdot \hat{n}) e^{i\vec{k} \cdot \vec{r}} . \quad (21)$$

Again I make use of the addition relation (A10), choosing the polar axis in the lab -frame coincident with the symmetry axis; I apply it twice, both on the $Y_l^0 = \sqrt{4\pi/(2l+1)} P_l^0$ above and on the plane wave, expanded as (17). Paying the price to increase the number of sums, equation (21) becomes

$$\begin{aligned} \Theta &= \sum_{l,m=-l}^l (-i)^l \frac{4\pi}{2l+1} Y_l^m(\hat{n}) \cdot \sum_{l',m'=-l'}^{l'} i^{l'} 4\pi Y_{l'}^{m'}(\hat{r}) \cdot \\ &\cdot \int \frac{k_+ dk_+ dk_z}{(2\pi)^3} \Theta_l(\eta, k_+, k_z) j_{l'}(kr) \int d\phi_{\hat{k}} Y_l^{m*}(\hat{k}) Y_{l'}^{m'*}(\hat{k}) , \end{aligned} \quad (22)$$

where of course $k^2 = k_+^2 + k_z^2$ and $r^2 = r_+^2 + r_z^2$. Now, it is manifest that the integral in $d\phi_{\hat{k}}$ kills everything except for the $m' = -m$ terms; thus, the phase of $Y_{l'}^{m'}(\hat{r})$ precisely fits together with the phase of $Y_l^m(\hat{n})$, making them relative. Writing in full the spherical harmonics, the final result is:

$$\begin{aligned} \Theta &= \sum_{l,m=-l}^l (-i)^l P_l^m(\hat{n} \cdot \hat{z}) e^{im(\phi_{\hat{n}} - \phi_{\hat{r}})} \sum_{l' \geq |m|}^{l'} i^{l'} (2l'+1) P_{l'}^{-m}(\hat{r} \cdot \hat{z}) \cdot \\ &\cdot \int \frac{k_+ dk_+ dk_z}{4\pi^2} \Theta_l(\eta, k_+, k_z) j_{l'}(kr) P_l^{-m}(\hat{k} \cdot \hat{z}) P_{l'}^m(\hat{k} \cdot \hat{z}) . \end{aligned} \quad (23)$$

It is useful to note that writing $\vec{k} \cdot \vec{r} = \vec{k}_+ \cdot \vec{r}_+ + k_z z$ and extracting the exponential regarding the last term from the integral in $d\phi_{\hat{k}}$, the expression (23) may be simplified:

$$\Theta = \sum_{l,m=-l}^l (-i)^l P_l^m(\hat{n} \cdot \hat{z}) e^{im(\phi_{\hat{n}} - \phi_{\hat{r}})} \sum_{l' \geq |m|} i^{l'} (2l' + 1) P_{l'}^m(0) P_{l'}^{-m}(0) \cdot \int \frac{k_+ dk_+ dk_z}{4\pi^2} \Theta_l(\eta, k_+, k_z) e^{ik_z z} j_{l'}(k_+ r_+) P_l^{-m}(\hat{k} \cdot \hat{z}) ; \quad (24)$$

note that the sum over l' is restricted to the even $l' + m$ terms because of equation (A9).

As an alternative approach, one can give up the expansion of the plane wave in (21), and express its argument as $\vec{k} \cdot \vec{r} = k_+ r_+ \cos(\phi_{\hat{k}} - \phi_{\hat{r}}) + k_z z$. As above, the phase of $Y_l^{m*}(\hat{k})$ is $e^{-im\phi_{\hat{k}}} = e^{im(\phi_{\hat{r}} - \phi_{\hat{k}})} \cdot e^{-im\phi_{\hat{r}}}$; the second factor comes out of the integral, and again fits together with the corresponding phase of $Y_l^m(\hat{n})$. The advantage of this approach is that the integral in $d\phi_{\hat{k}}$ has a note form and the result is:

$$\Theta = \sum_{l,m=-l}^l (-i)^l P_l^m(\hat{n} \cdot \hat{z}) \cdot e^{im(\phi_{\hat{n}} - \phi_{\hat{r}})} \int \frac{k_+ dk_+ dk_z}{(2\pi)^3} e^{ik_z z} \Theta_l(\eta, k_+, k_z) P_l^{-m}(\hat{k} \cdot \hat{z}) \mathbf{J}\mathbf{E}_+(m, k_+ r_+) , \quad (25)$$

where the function $\mathbf{J}\mathbf{E}_+$ is a combination of the Anger and Weber functions, defined in appendix B.

The expressions corresponding to (23,24) and (25) for an infinite cylindrical structure are simpler because of the effect of the Dirac delta; it eliminates the dependence on z , reducing the argument of the exponential in (21) to $i\vec{k}_+ \cdot \vec{r}_+$. Also the Legendre polynomials into the integral in $d\phi_{\hat{k}}$ have now to be calculated for $\hat{k} \cdot \hat{z} = 0$, their values being found using (A8); from (A9) only the terms with even $l + m$ and $l' + m$ (and therefore $l + l'$) survive. Thus, the expression for Θ in this case is similar to (24), but simpler:

$$\Theta = \sum_{l,m=-l}^l P_l^m(\hat{n} \cdot \hat{z}) P_l^{-m}(0) e^{im(\phi_{\hat{n}} - \phi_{\hat{r}})} \sum_{l' \geq |m|} (-1)^{l+(l+l')/2} (2l' + 1) \cdot P_{l'}^m(0) P_{l'}^{-m}(0) \cdot \int \frac{k_+ dk_+}{2\pi} \Theta_l(\eta, k_+) j_{l'}(k_+ r_+) \quad (\text{even } l + m, l' + m, l + l') . \quad (26)$$

In the second approach

$$\Theta = \sum_{l,m=-l}^l (-i)^l P_l^m(\hat{n} \cdot \hat{z}) P_l^{-m}(0) \cdot e^{im(\phi_{\hat{n}} - \phi_{\hat{r}})} \int \frac{k_+ dk_+}{4\pi^2} \Theta_l(\eta, k_+) \mathbf{J}\mathbf{E}_+(m, k_+ r_+) . \quad (27)$$

Let us check the geometric meanings of the above expressions. First note how the cylindrical symmetry caused complications, both in the geometric and integral quantities, with respect to the spherical case. However, again the dependence on \hat{n} and \hat{r} has been separated and factored out. The symmetry forces the phases of the harmonics with argument \hat{n} and \hat{r} to be relative: for $r_+ \neq 0$, the perturbation depends, together with the angle between the symmetry axis and \hat{n} , on the direction of the projection of \hat{n} on the equatorial plane with respect to \hat{r}_+ , as it is intuitive in a cylindrical problem; the pure Doppler contribution from the peculiar velocity of photons and baryons (Θ_1) may be easily recognized in the $l = 1, m = 1$ terms. If \vec{r} lies on the symmetry axis itself the $\mathbf{J}\mathbf{E}_+$ function in (25) and (27) reduces simply to $2\pi\delta_{m0}$, as shown in appendix B. As a final intuitive feature, note how in the case $\hat{n} \parallel \hat{z}$, the CMB perturbation for an infinitely long seed possesses a parity symmetry, $\hat{n} \rightarrow -\hat{n}$, since all the $m \neq 0$ terms vanish, making l and l' even.

Let us face now the CMB polarization from cylindrical sources. As in the previous section, the E_l coefficients come out of the integral in $d\phi_{\hat{k}}$ and the tensor harmonics are expressed as in (14). Then the polarization matrices in the \hat{k} -frame have to be expressed in terms of the corresponding ones in the lab -frame: $\mathbf{M}_{\pm}^{\hat{k}} = e^{\mp 2i\alpha_{\hat{k}}} \mathbf{M}_{\pm}$; as before $\alpha_{\hat{k}}$ is the angular coordinate of the projection of the \hat{k} versor on the plane orthogonal to \hat{n} . It is indicated differently from (15) because of the following reason. In the previous section we were dealing with spherical perturbations; no matter of how the lab -frame axes were oriented. This freedom allowed us to orient the polar axis as \hat{n} , so that $\alpha_{\hat{k}}$ was simply related to the ϕ coordinate of \hat{k} . Now things are different: the perturbation source has a preferred axis, and the equatorial plane is therefore different from the polarization plane (orthogonal to \hat{n}); consequently, $\alpha_{\hat{k}}$ depends on $\phi_{\hat{k}}$ in a less simple way, as I write below, and this complicates the computations of course.

Highlighting again the integral in $d\phi_{\hat{k}}$, the quantities in (4) take the form

$$(Q \pm iU)\mathbf{M}_{\pm} = \sum_{l \geq 2} \int \frac{k_+ dk_+ dk_z}{(2\pi)^3} E_l(\eta, k_+, k_z) \int d\phi_{\hat{k}} (-i)^l \sqrt{\frac{(l-2)!}{(l+2)!}} P_l^2(\hat{n} \cdot \hat{k}) e^{i(\vec{k} \cdot \vec{r} \mp 2\alpha_{\hat{k}})} \mathbf{M}_{\pm} . \quad (28)$$

In spite of its innocent appearance, the integral in $d\phi_{\hat{k}}$ is not so available for extracting the dependence on \hat{n} as in the previous cases. This is due to the expression of $\alpha_{\hat{k}}$; according to the definition above, and taking as reference axis the intersection between the planes orthogonal to \hat{n} and \hat{z} , its expression is

$$\cos \alpha_{\hat{k}} = \frac{\hat{n} \times \hat{z} \cdot \hat{k}}{|\hat{n} \times \hat{z}| \sqrt{1 - (\hat{k} \cdot \hat{n})^2}} . \quad (29)$$

Thus, $\alpha_{\hat{k}}$ is related to $\phi_{\hat{k}}$ by the following relation, that may be easily verified:

$$\cos \alpha_{\hat{k}} = \cos \phi_{\hat{k}} \sqrt{\frac{1 - (\hat{k} \cdot \hat{z})^2}{1 - (\hat{k} \cdot \hat{n})^2}} . \quad (30)$$

Unfortunately, (in my knowledge) there is no simple treatment of the angular integral in (28) with $\alpha_{\hat{k}}$ given by (30). However, there are some interesting and useful particular cases in which computations are simpler. First, suppose that the photon propagation direction \hat{n} is parallel to the symmetry axis. Thus $\alpha_{\hat{k}} = \phi_{\hat{k}}$, (15) holds, and the Legendre polynomials can be extracted from the integral in $d\phi_{\hat{k}}$, since now $\hat{n} = \hat{z}$. In the first approach all the task consists in expanding the exponential in (28), while the second is straightforward. The integral precisely kills everything except for the $m = \mp 2$ terms:

$$\begin{aligned} (Q \pm iU)\mathbf{M}_{\pm} &= \mathbf{M}_{\pm} e^{\mp 2i\phi_{\hat{r}}} \cdot \sum_{l \geq 2} (-i)^l \sqrt{\frac{(l-2)!}{(l+2)!}} \cdot \sum_{l' \geq 2} i^{l'} (2l' + 1) P_{l'}^{\mp 2}(\hat{r} \cdot \hat{z}) \cdot \\ &\cdot \int \frac{k_+ dk_+ dk_z}{4\pi^2} E_l(\eta, k_+, k_z) j_{l'}(kr) P_l^2(\hat{k} \cdot \hat{z}) P_{l'}^{\pm 2}(\hat{k} \cdot \hat{z}) = \\ &= \mathbf{M}_{\pm} e^{\mp 2i\phi_{\hat{r}}} \cdot \sum_{l \geq 2} (-i)^l \sqrt{\frac{(l-2)!}{(l+2)!}} \cdot \sum_{l' \geq 2} i^{l'} (2l' + 1) P_{l'}^{\mp 2}(0) P_{l'}^{\pm 2}(0) \cdot \\ &\cdot \int \frac{k_+ dk_+ dk_z}{4\pi^2} E_l(\eta, k_+, k_z) e^{ik_z z} j_{l'}(k_+ r_+) P_l^2(\hat{k} \cdot \hat{z}) , \quad (\text{valid for } \hat{n} = \hat{z}) , \end{aligned} \quad (31)$$

$$(Q \pm iU)\mathbf{M}_{\pm} = \mathbf{M}_{\pm} e^{\mp 2i\phi_{\hat{r}}} .$$

$$\cdot \sum_{l \geq 2} (-i)^l \sqrt{\frac{(l-2)!}{(l+2)!}} \cdot \int \frac{k_+ dk_+ dk_z}{(2\pi)^3} e^{ik_z z} E_l(\eta, k_+, k_z) P_l^2(\hat{k} \cdot \hat{z}) \mathbf{J}\mathbf{E}_+(\pm 2, k_+ r_+) , \quad (\text{valid for } \hat{n} = \hat{z}) . \quad (32)$$

This corresponds to the case sketched in the upper panel of figure 2, where the propagation direction is parallel to the symmetry axis. As in the spherical case, orienting the lab -axis as in the figure (so that $\phi_{\hat{r}} = 0$) yields an equal contribution from the \pm terms; the polarization is given by a pure Q term, giving the difference between the temperature fluctuations of the light polarized in the directions shown in the upper panel of figure 2; also, $\alpha = 0$ in (8), meaning that the polarization direction lies on the plane formed by \hat{n} and \hat{z} (and it is orthogonal to \hat{n} of course). The same quantities for an infinite cylindrical seed are easily gained using the Dirac delta (the sum is restricted to even l and l' from (A9)):

$$\begin{aligned} (Q \pm iU)\mathbf{M}_{\pm} &= \mathbf{M}_{\pm} e^{\mp 2i\phi_{\hat{r}}} \cdot \sum_{l \geq 2} \sqrt{\frac{(l-2)!}{(l+2)!}} P_l^2(0) \cdot \sum_{l' \geq 2} (-1)^{(l+l')/2} (2l' + 1) P_{l'}^{\mp 2}(0) P_{l'}^{\pm 2}(0) \cdot \\ &\cdot \int \frac{k_+ dk_+}{2\pi} E_l(\eta, k_+) j_{l'}(k_+ r_+) , \quad (\text{valid for } \hat{n} = \hat{z} \text{ even } l, l') , \end{aligned} \quad (33)$$

$$(Q \pm iU)\mathbf{M}_{\pm} = \mathbf{M}_{\pm} e^{\mp 2i\phi_{\hat{r}}}.$$

$$\cdot \sum_{l \geq 2} (-1)^{l/2} \sqrt{\frac{(l-2)!}{(l+2)!}} P_l^2(0) \cdot \int \frac{k_+ dk_+}{4\pi^2} E_l(\eta, k_+) \mathbf{J}\mathbf{E}_+(\pm 2, k_+ r_+) \quad , \quad (\text{valid for } \hat{n} = \hat{z}, \text{ even } l) \quad . \quad (34)$$

Just like the spherical case, photons propagating exactly *on* the symmetry axis have to be not polarized, since no preferred axis exists on the polarization plane. Let's check that the above results are consistent with this geometric expectation. In equations (31) and (33) this is manifest because the only Bessel function that would survive on the axis ($r_+ = 0$) would be j_0 , but it's not present, since $l' \geq 2$. For what concerns equations (32) and (34), the $\mathbf{J}\mathbf{E}_+$ function in $r_+ = 0$ is trivially 0 as is evident from (B6).

There is another case of interest for an infinite cylindrical structure: precisely when the \hat{n} direction is orthogonal to the axis. In this case the polarization plane and the equatorial plane are orthogonal; than it's easy to see that $\alpha_{\hat{k}}$ is $\tilde{\alpha}$ or $\tilde{\alpha} + \pi$ where the constant $\tilde{\alpha}$ is simply the angular coordinate of the projection of the equatorial plane into the polarization one: this is simply because, for the effect of the Dirac delta, the integration is confined into the equatorial plane $k_z = 0$. A necessary step here is to use a note expansion of the second order Legendre polynomial in term of the elementary ones

$$P_l^2(\hat{k} \cdot \hat{n}) = \sum_{j \leq l} a_{jl} P_j(\hat{k} \cdot \hat{n}) \quad , \quad (35)$$

where the coefficients a_{jl} are defined in appendix B, equation (A12). The arguments widely applied in this section lead to the following expressions of this interesting case:

$$(Q \pm iU)\mathbf{M}_{\pm} = \mathbf{M}_{\pm} e^{\mp 2i\tilde{\alpha}} \cdot \sum_{l \geq 2} \sqrt{\frac{(l-2)!}{(l+2)!}} \sum_{j, m=-j}^j a_{jl} P_j^m(0) P_j^{-m}(0) e^{im(\phi_{\hat{n}} - \phi_{\hat{r}})} \cdot \sum_{l' \geq |m|} (-1)^{l+(l'+l)/2} (2l'+1) \cdot P_{l'}^m(0) P_{l'}^{-m}(0) \cdot \int \frac{k_+ dk_+}{2\pi} E_l(\eta, k_+) j_{l'}(k_+ r_+) \quad , \quad (\text{valid for } \hat{n} \cdot \hat{z} = 0, \text{ even } j+l, l+m, l'+m, l+l') \quad , \quad (36)$$

$$(Q \pm iU)\mathbf{M}_{\pm} = \mathbf{M}_{\pm} e^{\mp 2i\tilde{\alpha}} \cdot \sum_{l \geq 2} (-i)^l \sqrt{\frac{(l-2)!}{(l+2)!}} \sum_{j, m=-j}^j a_{jl} P_j^m(0) P_j^{-m}(0) e^{im(\phi_{\hat{n}} - \phi_{\hat{r}})} \cdot \int \frac{k_+ dk_+}{4\pi^2} E_l(\eta, k_+) \mathbf{J}\mathbf{E}_+(m, k_+ r_+) \quad , \quad (\text{valid for } \hat{n} \cdot \hat{z} = 0); \quad (37)$$

the restriction to the sum in (36) comes from the properties of the expansion coefficients a_{jl} in (A12) and again from (A9). Despite of the large number of sums, equation (36) is workable because all the Legendre polynomials are calculated in the equatorial plane, $(\hat{n} \cdot \hat{z}) = (\hat{r} \cdot \hat{z}) = (\hat{k} \cdot \hat{z}) = 0$; it will be used for the numerical integrations in section V. Both the expressions explicitly show the symmetry of the seed; choosing the axes on the polarization plane parallel and orthogonal to the symmetry axis (so that $\tilde{\alpha} = 0$) implies that (36) and (37) give no distinction between the \pm modes, giving again a pure Q term; thus the polarization direction lies in the equatorial plane, as displayed in the upper panel of figure 2. As the very final observation, note that, in contrast to the case $\hat{n} = \hat{z}$, now photons propagating away from the symmetry axis at $r_+ = 0$ *can* be polarized; a numerical demonstration of this occurrence will be given in section V. Physically this is because there is a preferred axis on the polarization plane, the symmetry axis itself; formally, now the $m = j = 0$ term is admitted, so that j_0 at $r_+ = 0$ in (36) and $\mathbf{J}\mathbf{E}_+ = 2\pi\delta_{m0}$ in (37) survive; it is straightforward to write down the polarization tensor in this particular case:

$$(Q \pm iU)\mathbf{M}_{\pm} = \mathbf{M}_{\pm} e^{\mp 2i\tilde{\alpha}} \cdot \sum_{l \geq 2} (-1)^{l/2} \sqrt{\frac{(l-2)!}{(l+2)!}} \sum_{j \geq l} a_{jl} [P_j(0)]^2 \cdot \int \frac{k_+ dk_+}{2\pi} E_l(\eta, k_+) \quad (\text{even } l, j) \quad ; \quad (38)$$

it depends on nothing more, except for the nature of the infinite seed, encoded in the E_l coefficients.

The equations I have developed here and in the previous section describe CMB perturbations, both for temperature and polarization, around symmetric seeds at a given time specified by η . In the next section I show how to get their appearance on the CMB sky.

IV. POLARIZATION AND TEMPERATURE ANISOTROPIES

The expressions in the previous sections describe the CMB polarization and temperature *perturbations* around a symmetric structure, as a function of the conformal time η and the geometry of the seed itself. At any time, if a perfect CMB detector is placed around one of the seed analyzed, the measure of the CMB perturbation carried by a photon propagating on a direction \hat{n} would give the appropriate result from the above formulas.

Now let's face the computation of the CMB *anisotropy* from a symmetric seed. This requires the convolution of the CMB perturbation with the decoupling history of the universe. According to the current scenario, CMB photons were last scattered far from us in spacetime, when the scale factor was approximatively one thousandth than now. Such process is described by the last scattering probability between η and $\eta + d\eta$, function of several cosmological parameters and of the time of course; its expression in terms of the differential optical depth $\tau(\eta)$ (see section V) is very simple:

$$P(\eta) = \dot{\tau} e^{-\tau} . \quad (39)$$

With the appropriate numbers, the last scattering probability peaks on a spherical corona around us moving away with the light speed of course; it has present radius and thickness of about $6000h^{-1}$ and $10h^{-1}$ comoving Mpc respectively; for its thinness this zone is called last scattering surface (LSS). Since it is useful here, I recall that using the conformal time as temporal coordinate is also convenient since a photon last scattered at η has to travel a comoving distance $\eta_0 - \eta$ to reach our spacetime position, indicated in the following with the subscript $_0$.

As mentioned in the introduction, the most known class of primordial perturbations is Gaussian and (nearly) scale-invariant; a simplification allowed by this statistics is that the CMB anisotropies have the same spectrum regardless of the position of the observer (Cosmic Variance subtracted of course [17]). The seeds analyzed here represent a radically different CMB anisotropy source; technically speaking they are non-Gaussian and non-scale-invariant. As a consequence of this, the *position* of the source along the photons path becomes here a physical degree of freedom, and the classification of the various possibilities is essential to predict how the CMB signal from a symmetric seed could appear.

Let us start from the spherical symmetry. As sketched in the lower panel of figure 1, the CMB anisotropies are completely specified by the comoving distance d between the seed center and the LSS peak: the latter is defined as the point from which we receive CMB photons with highest probability (peak of $P(\eta)$) on the direction \hat{n}_c corresponding to the center of the spherical seed; the observer is far on the right and receives on a direction \hat{n} the CMB photons last scattered inside the spherical perturbation, with probability sketched as a Gaussian in the figure. The whole signal is symmetric with respect to rotations around \hat{n}_c . Also it is convenient to define the useful angle θ by

$$\hat{n} \cdot \hat{n}_c = \cos \theta ; \quad (40)$$

it is simply the angle between the photon propagation direction \hat{n} and the direction corresponding to photons coming from the center of the spherical seed in the sky. A photon last scattered at η with direction \hat{n} carries a CMB perturbation computable with the formulas developed in the previous section, that require its radial coordinate r ; the latter is completely fixed by η , d and θ :

$$r = [(d + \eta_0 - \eta_{LSS})^2 + (\eta_0 - \eta)^2 - 2(d + \eta_0 - \eta_{LSS})(\eta_0 - \eta) \cos \theta]^{1/2} , \quad (41)$$

where η_{LSS} and η_0 mean LSS peak and present conformal times respectively; in fact, since $\eta_0 - \eta$ is just the comoving causal distance covered by a photon last scattered at η and reaching us today, gaining equation (41) is matter of simple trigonometry, see figure 1. This completes the spherically symmetric case. Once we have specified d , gaining the CMB polarization and temperature anisotropies from a spherical seed means performing line of sight integrations for each direction specified by θ , as it is exposed below. Of course, the appearance on the sky of the CMB temperature and polarization anisotropies from one spherical seed is circular; more interesting, while nothing forbids photons coming on the \hat{n}_c direction to carry a temperature perturbation, the geometric constraint treated in section II forces them to be not polarized. A nice example of this occurrence can be found in [1].

Let's face now the case of CMB anisotropies coming from cylindrically symmetric seeds. First of all, let's define the plane Π containing the seed symmetry axis and our observation point: the signal is of course symmetric with respect to reflections on this plane. Also let's define a Π orthogonal versor, \hat{n}_Π , and one along the symmetry axis, \hat{z} , regardless of their direction. Take now a representative point \vec{C} on the symmetry axis; in the spherical case it was the sphere's center, but here, in principle, it could be any point along the axis: inside the seeds itself, or the axis intersection with the LSS peak, or ultimately the point of minimal distance from the observation point. Let's define \hat{n}_C as the direction of photons coming from \vec{C} and D its comoving distance from the LSS peak (of course $\hat{n}_\Pi \cdot \hat{n}_C = 0$); these simple geometric quantities are displayed in figure 2, bottom panel. Now take a photon last scattered at η on a direction \hat{n} , described with the usual angles θ and ϕ in the frame defined by $\hat{e}_3 = \hat{z}$, $\hat{e}_1 = \hat{n}_\Pi$ and $\hat{e}_2 = \hat{z} \times \hat{n}_\Pi$ (only $|\pi/2 - \phi|$ would be necessary, since the signal does not change for reflections on Π , look at figure 2). Let's define for a moment \vec{P} and \vec{O} to be the photon scattering point and the observation point as seen by the frame centered in \vec{C} :

$$\vec{P} = r_+ \cos \phi \hat{n}_\Pi + r_+ \sin \phi \hat{z} \times \hat{n}_\Pi + z \hat{z} , \quad (42)$$

$$\vec{O} = (D + \eta_{LSS}) \cdot \hat{n}_C ; \quad (43)$$

in order to employ the equations developed in the previous section we need to know r_+ and z . This is easily done by expressing \vec{P} as seen in a system with the same axes orientation but centered in \vec{O} :

$$\vec{P}' = -(\eta_0 - \eta) \cdot \hat{n} = \vec{P} - \vec{O} . \quad (44)$$

This fixes the quantities needed:

$$\begin{aligned} r_+ = & [(\eta_0 - \eta)^2 \sin^2 \theta + (D + \eta_{LSS})^2 [(\hat{n}_C \cdot \hat{z} \times \hat{n}_\Pi)^2 + (\hat{n}_C \cdot \hat{n}_\Pi)^2] - \\ & - 2 \sin \theta (\hat{n}_C \cdot \hat{n}_\Pi \cos \phi + \hat{n}_C \cdot \hat{z} \times \hat{n}_\Pi \sin \phi) (\eta_0 - \eta) (D + \eta_{LSS})]^{1/2} , \end{aligned} \quad (45)$$

$$z = -(\eta_0 - \eta) \cos \theta + (\eta_{LSS} + D) \hat{n}_C \cdot \hat{z} . \quad (46)$$

As expected, the cylindrical symmetry has introduced an angular variable more than the spherical case. The quantities r_+ and z defined above allow to employ the formulas developed in the previous section to compute the CMB anisotropy carried by the photon last scattered at η on the direction \hat{n} ; of course, for an infinite cylindrical seed only the r_+ coordinate is necessary. While anisotropies in the spherical case are characterized by a circular imprint, here their shape may vary with the orientation of the symmetry axis. If it coincides with \hat{n}_C , thus including the observation point, the imprint is circular around it, and again polarization anisotropies are absent on the direction corresponding to the symmetry axis itself. In any other case, both polarization and temperature anisotropies would appear symmetric around a *line* in the sky, projection of the seed symmetry axis on the celestial sphere.

Finally, the CMB anisotropies both for the spherical and cylindrical cases are obtained through a line of sight integration along the photon's path, convolved with the last scattering probability (see [7]):

$$\Theta(\eta_0, \text{here}, \hat{n}) = \int_0^{\eta_0} [(\Theta + \Psi)(\eta, \text{arg}, \hat{n})P(\eta) + (\dot{\Psi} - \dot{\Phi})(\eta, \text{arg}, \hat{n})e^{-\tau}] d\eta , \quad (47)$$

$$(Q \pm iU)(\eta_0, \text{here}, \hat{n})\mathbf{M}_\pm = \int_0^{\eta_0} (Q \pm iU)(\eta, \text{arg}, \hat{n})\mathbf{M}_\pm P(\eta) d\eta ; \quad (48)$$

at each η , (41) and (45,46) give the necessary arguments (*arg*) to compute the CMB perturbations. Ψ accounts for the Sachs-Wolfe effect, due to the work spent by the photon climbing out of the potential well (or hill) in which it was last scattered; the time derivatives account for the integrated Sachs-Wolfe effect, due to the work spent by the same photon crossing the density perturbations on the way toward us.

The following consideration introduces to the next section. As I have already mentioned, a symmetric seed could be a spatially limited structure, say a monopole or a bubble for the spherical case, or a string for the cylindrical case. Thus also the CMB anisotropy is spatially limited, since the evolution equations may transport the CMB perturbation at most at a sound horizon distance from the source. Therefore, if the perturbed zone does not intersects the LSS, meaning that it occupies a spacetime region where $P(\eta)$ is negligibly small, the terms Θ , Q and U above do not give contributions; in this situation, the seed can't signal its presence, except for the integrated Sachs-Wolfe effect if it lies within our Hubble sphere (a distinctive and fascinating signal in this case arise from cosmic strings [10]). Thus, in order to detect the genuine CMB signal from a symmetric spatially limited seed, we should be lucky with its spacetime location: it should intersect the LSS.

V. THE PEBBLES IN A POND

Let us apply the formulas developed in the previous sections. I plunge a toy symmetric source in the cosmic fluid at the initial time $\eta = 0$, computing its evolution by using the linear theory of the cosmological perturbations. At different times during the evolution, some pictures of the corresponding CMB polarization and temperature perturbations are taken. Finally, the computation of the line of sight integrals (47) and (48) simulates the CMB signal as it would appear in an high resolution observation.

First, let us define the initial density perturbations. For the spherical case, I take a potential energy condensation with a Gaussian shape extending on a comoving radial distance R :

$$\Psi(r, \eta = 0) = \mathcal{N} \exp \left[- \left(\frac{r}{R} \right)^2 \right] . \quad (49)$$

For the cylindrical case, I take an infinitely long seed, with a potential energy condensation on the equatorial plane characterized again by a Gaussian shape and extending on a scale R_+ :

$$\Psi(r_+, \eta = 0) = \mathcal{M} \exp \left[- \left(\frac{r_+}{R_+} \right)^2 \right]. \quad (50)$$

The normalization constants will be fixed below. The Fourier transforms are easily performed in the frame with origin in the center of the sources:

$$\Psi(k, \eta = 0) = \mathcal{N} \pi^{3/2} R^3 \exp \left[- \left(\frac{kR}{2} \right)^2 \right], \quad (51)$$

$$\Psi(k_+, \eta = 0) = \mathcal{M} \pi R_+^2 \exp \left[- \left(\frac{k_+ R_+}{2} \right)^2 \right]. \quad (52)$$

The evolution equations for fluid and CMB quantities may be obtained by the Boltzmann and linearized Einstein equations [13,2,7]. A standard CDM scenario is assumed, including cold dark matter (c), baryons (b), photons (γ) and three families of massless neutrinos (ν). All the equations in the following are written in Fourier space. The equations for the matter species are:

$$\dot{\delta}_c = -k v_c - 3k^2 \dot{\Phi}, \quad \dot{v}_c = -\frac{\dot{a}}{a} v_c + k \Psi, \quad (53)$$

$$\dot{\delta}_b = -k v_b - 3k^2 \dot{\Phi}, \quad \dot{v}_b = -\frac{\dot{a}}{a} v_b + k \Psi + \frac{4\rho_\gamma}{3\rho_b} a n_e \sigma_T (v_\gamma - v_b), \quad (54)$$

where $\delta \equiv (\delta\rho/\rho)$ and $\dot{\tau} = a x_e n_e \sigma_T$ is the differential optical depth; n_e is the electron number density and x_e is the ionization fraction (see the last work in reference [7] for useful fitting formulas). Photon equations involve each multipole in the expansions (3) and (4):

$$\dot{\Theta}_0 = -\frac{k}{3} \Theta_1 - \dot{\Phi}, \quad \dot{\Theta}_1 = k \Theta_0 - \frac{2}{5} k \Theta_2 + \dot{\tau} (v_b - \Theta_1) + k \Psi, \quad (55)$$

$$\dot{\Theta}_2 = \frac{2}{3} k \Theta_1 - \frac{3}{7} k \Theta_3 - \dot{\tau} \left(\frac{9}{10} \Theta_2 - \frac{\sqrt{6}}{10} E_2 \right), \quad \dot{E}_2 = -\frac{\sqrt{5}}{7} k E_3 - \dot{\tau} \left(\frac{1}{10} \Theta_2 + \frac{2}{5} E_2 \right), \quad (56)$$

and for $l \geq 3$:

$$\dot{\Theta}_l = k \left[\frac{l}{2l-1} \Theta_{l-1} - \frac{l+1}{2l+3} \Theta_{l+1} \right] - \dot{\tau} \Theta_l, \quad \dot{E}_l = k \left[\frac{\sqrt{l^2-4}}{2l-1} E_{l-1} - \frac{\sqrt{(l+1)^2-4}}{2l+3} E_{l+1} \right] - \dot{\tau} E_l. \quad (57)$$

In Newtonian gauge the lowest multipoles are linked to the photon fluid quantities by $\delta_\gamma = 4\Theta_0$, $v_\gamma = \Theta_1$ and $\pi_\gamma = 12\Theta_2/5$. Massless neutrinos can be treated as photons without the polarization and Thomson scattering terms. Finally, the equations for the gravitational potentials are:

$$k^2 \Phi = 4\pi G a^2 \left[\rho_c \delta_c + \rho_b \delta_b + \rho_\gamma \delta_\gamma + \rho_\nu \delta_\nu + \frac{3}{k} \frac{\dot{a}}{a} \left(\rho_c v_c + \rho_b v_b + \frac{4}{3} \rho_\gamma v_\gamma + \frac{4}{3} \rho_\nu v_\nu \right) \right], \quad (58)$$

$$-k^2 (\Psi + \Phi) = \frac{8\pi G}{3} (\rho_\gamma \pi_\gamma + \rho_\nu \pi_\nu). \quad (59)$$

As it is known [13,2], at early times the above system can be solved by using the tight coupling approximation between photons and baryons. The multipole equations are expanded in powers of $k/\dot{\tau} \ll 1$. The only zero order terms are Θ_0 and Θ_1 from (54,55), and obey the following equations:

$$\dot{\Theta}_0 = -\frac{k}{3} \Theta_1 - \dot{\Phi}, \quad \frac{d}{d\eta} \left[\left(1 + \frac{3\rho_b}{4\rho_\gamma} \right) \Theta_1 \right] = k \Theta_0 + k \left(1 + \frac{3\rho_b}{4\rho_\gamma} \right) \Psi, \quad (60)$$

where Θ_1 is assumed to coincide with v_b to the lowest order. Increasing the order in $k/\dot{\tau}$ the higher multipoles are given by

$$\Theta_2 = \frac{k}{\dot{\tau}} \frac{8}{9} \Theta_1, \quad E_2 = -\frac{\sqrt{6}}{4} \Theta_2, \quad (61)$$

$$\Theta_l = \frac{k}{\dot{\tau}} \frac{l}{2l-1} \Theta_{l-1}, \quad E_l = \frac{k}{\dot{\tau}} \frac{\sqrt{l^2-4}}{2l-1} E_{l-1}. \quad (62)$$

I integrate in time the system (60, 61,62) until $k/\dot{\tau} = .1$ occurs, thereafter integrating the complete equations; of course, care is taken that the results do not depend at all on this choice.

I take adiabatic initial conditions: at early times $\delta_c = \delta_b = 3\delta_\gamma/4 = 3\delta_\nu/4$ (all the velocity are initially zero) and the second member in equation (58) at $\eta = 0$ is proportional for each Fourier mode to the initial perturbation spectrum (51) or (52); in order to make the following results more clear, the latter is normalized with the density contrast δ taken in the center of the seed at decoupling. This choice is not dependent on the particular gauge chosen here, since equation (58) is gauge invariant [2]. In the CMB equations, everything is initially zero except for the lowest multipole of the temperature perturbation [13]:

$$\Theta_0(0) = -2\Psi(0). \quad (63)$$

The background evolution is driven by the Einstein equation

$$\frac{\dot{a}^2}{a^2} = \frac{8\pi G}{3} a^2 \sum_a \rho_a, \quad (64)$$

where the index a runs over all the fluid species. Now the computation system is ready. The background parameters describe a standard CDM model ($\Omega_0 = 1, h = .5, \Omega_b = 0.05, \Omega_{CDM} = 1 - \Omega_b$).

Figure 3 shows the time evolution of the CMB temperature perturbation from the spherical seed. The chosen comoving size is $R = 10h^{-1}$ Mpc, that is well below the effective horizon at decoupling, (approximately $100h^{-1}$ Mpc). The radial profile is shown, and the temperature perturbation has been computed from equation (13) for photons propagating perpendicularly to the radial direction, as indicated. The sum converges very rapidly: the heavy line shows the result from the first ten multipoles, while the light one, almost indistinguishable, indicates the result from the only $l = 0$ multipole in (13). The figure points out the wave-like behavior of the CMB perturbations. The initial condition (panel *a*) remains unchanged until the horizon crossing, that occurs nearly at equivalence for the chosen size. At this time, in panel *b*, baryons tend to fall into the potential well, and the perturbation amplitude grows. After that, in panel *c*, an opposite oscillation due to the pressure reaction takes place, pushing the perturbation away from the center. Finally, in panel *d* the perturbation is shown just before decoupling: the oscillatory behavior caused a temperature perturbation wave that is propagating outward. The wave crest is just at the position of the sound horizon at the time displayed. This phenomenology is analogous in figure 4, where the polarization amplitude, computed using equation (18), is shown. At the initial time no perturbation is visible, since all the Fourier modes are outside the horizon. At the horizon crossing the oscillations begin, producing a well visible polarization wave that travels outward with the CMB sound velocity. Note that, as an important distinction with respect to the temperature case, for the polarization there is no perturbation near the center, at small r . This is a practical realization of the geometric constraint exposed in section II: photons propagating radially in a spherical density field must be not polarized, since no preferred axis exists on the polarization plane.

Figures 5 and 6 show the same analysis on the cylindrical seed and remarkably the same undulatory phenomenology of the spherical case occurs. The size is $R_+ = 10h^{-1}$ Mpc and photons propagating perpendicularly to the symmetry and radial directions are considered, from equations (26) and (36). Again the sum converges very rapidly: the light line in figure 5 corresponds to the $l = 0$ terms in (26). At the horizon crossing, the competition between pressure and gravity generate CMB temperature and polarization waves propagating away from the symmetry axis. Just before decoupling, panels *d*, temperature and polarization waves are well visible a CMB sound horizon away from the axis of the cylindrical seed. As an interesting feature, note how in this case the polarization for photons scattered on the symmetry axis is non-vanishing: this is evident particularly in panel *c*. The central polarization amplitude is in any case smaller than the mean signal size, since for $r_+ \rightarrow 0$ in (36) only the $l = 0$ term survive.

Figure 7 shows the results of the line of sight integrals (47) and (48), where for simplicity only the spherical case is shown; I recall that θ is the angle between the line of sight and the one corresponding to the center of the seed. The importance of the different positions of the seed with respect to the LSS is evident: the solid line shows the signal if the spherical perturbation lies exactly on the last scattering surface, $d = 0$, while the dashed and dotted dashed lines corresponds to the cases $d = 30h^{-1}$ Mpc and $d = -30h^{-1}$ Mpc respectively. The general features pointed of the time evolution have been preserved. Simply, the CMB temperature and polarization waves propagating outward from the spherical seed have been snapped by the decoupling photons. The anisotropy waves extend on the scale of a CMB sound horizon at decoupling, that is roughly 1° in the sky. The temperature perturbation contains a central spot, that is absent in the polarization case.

It is important to point out the following considerations. First, note that the mean amplitude of the signal follows the known expectations [14] for a linear structure with size $L \leq H^{-1}$ and density contrast δ at decoupling: $\delta T/T \simeq \delta(L/H^{-1})^2$, roughly ten times stronger than the polarization signal. From the point of view of the dark matter distribution, the seed lies in the very central part of the graph, say $\theta \leq 10'$ (corresponding to less than $10h^{-1}$ Mpc in figure 3 and 4). Also the amplitude of the waves has the same mean magnitude of the signal coming from

the location of the seed; really, in the polarization from a spherical seed they are the very dominant component of the anisotropy. Thus they must be considered in any simulation aiming at the detection of this kind of signals. Also they could play some role in the structure formation around the seed, since they are physically made of photons and baryons. Besides, from an experimental point of view this undulatory occurrence could help the detection if structure like these ones should really exist. Indeed the CMB signal from a spatially limited seed is extended on the scale of a sound horizon at decoupling even if the size of the seed itself is smaller; therefore it appears as a series of sub-degree rings centered on the position of the seed; this can help to discriminate between the signals from point astrophysical sources from genuine cosmological seeds of primordial origin. Also, as it is evident from figure 7, a marked correlation exists between the temperature and polarization signals. Of course, this would improve the signal to noise ratio for high resolution instruments like Planck capable to detect both polarization and temperature anisotropy.

VI. CONCLUSION

At the present time, very high energy physics is still rather unknown and only theoretically approached. The breaking of high energy symmetries in the early universe may have left some traces of their occurrence, like topological defects or true vacuum bubbles. These relics act as seeds for polarization and temperature anisotropies in the cosmic microwave background (CMB), and this work aims at providing a general framework in order to predict their signal.

I have considered the cases of spherical and cylindrical symmetry of the perturbation source; no other specification characterizes the seed. I have obtained general formulas describing CMB polarization and temperature perturbations, as a function of time, generated by the most general structures characterized by the mentioned symmetries. The analysis regards both the pure CMB perturbation nearby the seeds and their CMB anisotropy as observed in our sky. Such expressions explicitly show several nice features to their own CMB imprint.

In spherical symmetry, the polarization and temperature perturbations depend geometrically on the scalar product $\hat{n} \cdot \hat{r}$, where the first is the photon propagation direction and the second the radial versor in the point where CMB is being measured. I give explicit expressions in which this dependence is factored out of the integral over the Fourier perturbations modes. In particular the polarization direction (orthogonal to \hat{n} of course) lies on the plane formed by \hat{n} and \hat{r} . As an important difference between polarization and temperature perturbations, the light propagating from the center of the seed is not polarized, since the radial propagation in spherical symmetry is an axial symmetric problem, so that no preferred axis exists for the polarization; instead nothing forbids a temperature perturbation.

In cylindrical symmetry the polarization and temperature perturbations depend on the products $\hat{n} \cdot \hat{z}$ and $\hat{r} \cdot \hat{z}$, where \hat{z} is the symmetry axis, as well as on the angular difference between the projections of \hat{n} and \hat{r} on the plane orthogonal to \hat{z} ; the $\hat{r} \cdot \hat{z}$ dependence is lost if the seed is invariant for translations along the symmetry axis (mentioned as infinite in the following). I give formal expressions showing these dependences, and extract them analytically from the Fourier integral in the cases of propagation parallel and orthogonal to the symmetry axis. In the first case the polarization direction lies on the plane formed by \hat{n} and \hat{z} ; as for the spherical case, photons traveling exactly on the symmetry axis are not polarized. In the second case, and for an infinite seed, the polarization direction is orthogonal to the symmetry axis.

For what concerns the CMB anisotropies as observed in our sky, they are computed with an usual line of sight integration, but the seeds considered here introduce additional variables with respect to the ordinary Gaussian case, that specify their position and orientation along the photons path toward us, characterizing their appearance on our CMB sky.

Polarization and temperature anisotropies from a spherical seed are circular and specified by the distance d between the seed center and the LSS peak. As a consequence of the geometric constraints summarized above, CMB polarization anisotropy is absent for photons coming from the center of the seed; on the other hand, nothing prevents them to possess a temperature perturbation.

Anisotropies from a cylindrical seed are specified by the distance D between a representative point on the symmetry axis and the LSS peak, as well as on the angular orientation of the symmetry axis itself on the plane containing it and the observation point. Anisotropies may appear in different ways. If the symmetry axis includes the observation point, what we would see is a circular imprint again; as in the spherical case, CMB polarization anisotropy is absent for photons coming from the center. In any other case, anisotropies would appear symmetric around a line in the sky, projection of the axis on the celestial sphere, thus giving the genuine sign of a cylindrical seed.

I have performed some numerical work on the formulas developed here, adopting toy symmetric sources in order to see the pure CMB processes at work with this kind of seed. The time evolution of the seed and of its corresponding CMB perturbation is performed from the initial time, and several pictures are taken before decoupling. The integrations highlight the undulatory behavior of the CMB perturbations. Just like a pebble in a pond, the oscillations occurring at the horizon crossing produce temperature and polarization perturbation waves that propagate outward with the CMB sound velocity. Consequently, the CMB anisotropies caused from structures like the ones analyzed here that intersect the last scattering surface extend at least on 1° in the sky, that is the angular scale corresponding to the CMB sound horizon at decoupling; the signals contain anisotropy waves, each one characterized by its own value of temperature and polarization perturbation. This component of the signal possesses the same magnitude of the one coming directly from the seed interior. The mean amplitude roughly follow the known expectations for a linear structure with size $L \leq H^{-1}$ and density contrast δ at decoupling: $\delta T/T \simeq \delta(L/H^{-1})^2$, roughly ten times stronger than the polarization signal, where H^{-1} is the size of the Hubble length at decoupling. The anisotropy waves coming out of a symmetric spatially limited seed are a unique proof that the seed itself existed well before

decoupling; thus, these waves could allow to distinguish relics from high energy processes of the early universe from point-like astrophysical sources, because of the angular extension and amplitude. Also, this phenomenology offers cross correlation possibilities for detectors like Planck capable to explore both temperature and polarization CMB sky.

Future works will deal with models of real symmetric structures, relics from high energy physics. These works aim at predicting their appearance on the CMB map itself before than on the anisotropy power spectrum. Their detection in the high resolution CMB maps provided by the Microwave Anisotropy Probe and Planck missions in the next decade would be an invaluable insight into the hidden sector of high energy physics.

ACKNOWLEDGMENTS

The first half of this work was performed at the NASA/Fermilab Astrophysics center. It was supported by the DOE and the NASA grant NAG 5-7092. I warmly thank the hospitality of the Theoretical Astrophysics Group. Also I wish to thank Luca Amendola and Franco Occhionero for constant encouragement. Finally, I am grateful to Luigi Danese and the astrophysics sector at SISSA/ISAS, where this work was completed.

APPENDIX A: SPHERICAL HARMONICS AND RELATED QUANTITIES

The spherical harmonics are expressed as usual as

$$Y_l^m(\theta, \phi) = \sqrt{\frac{(2l+1)(l-m)!}{4\pi(l+m)!}} P_l^m(\cos\theta) e^{im\phi} , \quad (\text{A1})$$

where the Legendre polynomials are defined by

$$P_l^m(x) = (-1)^m (1-x^2)^{m/2} \frac{d^m}{dx^m} P_l(x) , \quad P_l^{-m}(x) = (-1)^m \frac{(l-m)!}{(l+m)!} P_l^m(x) , \quad (m \geq 0) , \quad (\text{A2})$$

where $x = \cos\theta$. Legendre polynomials and spherical harmonics obey the orthogonality relations

$$\int_{-1}^1 dx P_l^m(x) P_{l'}^m(x) = \delta_{ll'} \frac{2}{2l+1} \frac{(l+m)!}{(l-m)!} , \quad \int \sin\theta d\theta d\phi Y_l^{m*}(\theta, \phi) Y_{l'}^{m'}(\theta, \phi) = \delta_{ll'} \delta_{mm'} , \quad (\text{A3})$$

and are eigenmodes of the parity operator:

$$P_l^m(-x) \rightarrow (-1)^{l+m} P_l^m(x) . \quad (\text{A4})$$

Legendre polynomials satisfy the following note recurrence relations:

$$(l-m)P_l^m(x) = x(2l-1)P_{l-1}^m(x) - (l+m-1)P_{l-2}^m(x) , \quad (\text{A5})$$

$$P_l^{m+2}(x) + \frac{2(m+1)x}{\sqrt{1-x^2}} P_l^{m+1}(x) + (l-m)(l+m+1)P_l^m(x) = 0 , \quad (\text{A6})$$

$$(1-x^2) \frac{dP_l^m}{dx} = -lxP_l^m(x) + (l+m)P_{l-1}^m(x) ; \quad (\text{A7})$$

they can be used to gain the value of any Legendre polynomials in $x = 0$:

$$P_0^0(0) = 1 , \quad P_1^0(0) = 0 , \quad P_1^1(0) = -1 , \quad P_2^1(0) = 0 , \\ (l-m)P_l^m(0) = -(l+m-1)P_{l-2}^m(0) , \quad P_l^{m+2}(0) = -(l-m)(l+m+1)P_l^m(0) . \quad (\text{A8})$$

Also note that

$$P_l^m(0) = 0 \quad \text{for odd } l+m . \quad (\text{A9})$$

In this work I have often used the addition relation for spherical harmonics, given by

$$P_l(\hat{n}_1 \cdot \hat{n}_2) = \frac{4\pi}{2l+1} \sum_{m=-l}^l Y_l^m(\hat{n}_1) Y_l^{m*}(\hat{n}_2) , \quad (\text{A10})$$

and the following useful integral relation, that may be verified easily using the addition relation itself:

$$\int d\Omega_{\hat{n}_1} P_l(\hat{n}_1 \cdot \hat{n}_2) P_{l'}(\hat{n}_1 \cdot \hat{n}_3) = \delta_{ll'} \frac{4\pi}{2l+1} P_l(\hat{n}_2 \cdot \hat{n}_3) . \quad (\text{A11})$$

Second order Legendre polynomials admit the following expansion [5]:

$$P_l^2(x) = \sum_{j \leq l} a_{jl} P_j(x) , \quad \text{where} \quad (\text{A12})$$

$$\begin{aligned} a_{jl} &= 0 \text{ for } j > l \text{ or } l + j \text{ odd} , \\ a_{jl} &= -2l(l-1)(2j+1)/(4l+2) \text{ for } l = j , \\ a_{jl} &= 2(2j+1) \text{ for } j < l \text{ and } l + j \text{ even} . \end{aligned} \quad (\text{A13})$$

The tensor spherical harmonics are defined in terms of the ordinary ones by

$${}_{\pm 2} Y_l^m(x) = \sqrt{\frac{(l-2)!}{(l+2)!}} \left[\partial_\theta^2 - \cot\theta \partial_\theta \mp \frac{2m}{\sin\theta} (\partial_\theta - \cot\theta) + \frac{m^2}{\sin^2\theta} \right] Y_l^m(\theta, \phi) ; \quad (\text{A14})$$

the normalization coefficient may vary in literature. Equation (14) is easily obtained in the following way. From (A6) one can immediately see that

$$\cot\theta \partial_\theta P_l(x) = -\frac{1}{2} P_l^2(x) - \frac{l(l+1)}{2} P_l(x) . \quad (\text{A15})$$

Also the equality

$$\partial_\theta^2 P_l(x) = \frac{x}{\sqrt{1-x^2}} P_l^1(x) + P_l^2(x) \quad (\text{A16})$$

holds by using elementary derivation. Using again (A6) for $m = 0$ and putting (A15) and (A7) together, the wanted equation is obtained:

$${}_2 Y_l^0(x) = \sqrt{\frac{2l+1}{4\pi} \frac{(l-2)!}{(l+2)!}} P_l^2(x) . \quad (\text{A17})$$

APPENDIX B: ANGER AND WEBER FUNCTIONS

This appendix contains some useful integration relations. Focus on the integral

$$\int_0^\pi \exp[\pm i(\nu\phi - \beta \sin\phi)] d\phi = \pi [\mathbf{J}_\nu(\beta) \pm i \mathbf{E}_\nu(\beta)] , \quad (\text{Re}\beta > 0) , \quad (\text{B1})$$

where \mathbf{J}_ν and \mathbf{E}_ν are the Anger and Weber functions respectively (see [6] for useful recurrence relations):

$$\mathbf{J}_\nu(z) = \frac{1}{\pi} \int_0^\pi \cos(\nu\theta - z \sin\theta) d\theta , \quad (\text{B2})$$

$$\mathbf{E}_\nu(z) = \frac{1}{\pi} \int_0^\pi \sin(\nu\theta - z \sin\theta) d\theta , \quad (\text{B3})$$

The two following equalities are easily gained using elementary integration algebra:

$$\int_0^{2\pi} \exp[\pm i(\nu\phi - \beta \sin \phi)] d\phi = \pi[\mathbf{J}_\nu(\beta) \pm i\mathbf{E}_\nu(\beta)] + \pi e^{\pm i\nu\pi}[\mathbf{J}_{-\nu}(\beta) \mp i\mathbf{E}_{-\nu}(\beta)] , \quad (\text{B4})$$

$$\int_0^{2\pi} \exp[\pm i(\nu\phi - \beta \sin \phi)] d\phi = e^{\pm i\nu\pi/2} \int_{-\pi/2}^{3\pi/2} \exp[\mp i(-\nu\phi + \beta \cos \phi)] d\phi . \quad (\text{B5})$$

If ν is integer, all the functions in the integrals are periodical on the 2π interval, so as the integrals above do not depend on the starting point. Thus the following equality holds:

$$\int_0^{2\pi} \exp[\pm i(-m\phi + \beta \cos \phi)] d\phi = \pi e^{\pm im\pi/2}[\mathbf{J}_m(\beta) \mp i\mathbf{E}_m(\beta)] + \pi e^{\mp i\nu\pi/2}[\mathbf{J}_{-m}(\beta) \pm i\mathbf{E}_{-m}(\beta)] = \mathbf{J}\mathbf{E}_\pm(m, \beta) ; \quad (\text{B6})$$

it's valid for $m = \nu$ integer and $\text{Re}\beta > 0$; the last equality is a pure definition. Note that in the particular case $\beta = 0$, the above expression reduces simply to $2\pi\delta_{m0}$.

- [1] Baccigalupi C. 1998, Ap.J 496 615, astro-ph/9711095; Amendola L., Baccigalupi C. & Occhionero F. 1998 Ap.J. Lett. 492, L5; Baccigalupi C. 1999, in preparation
- [2] Bardeen J.M. 1980 Phys.Rev.D 22, 1882; Kodama I. & Sasaki M. 1984 Progr. of Theor.Phys.Supp. 78, 1
- [3] Born M. & Wolfe E. *Principles of optics* , Pergamon Press 1980
- [4] Kolb E.W. 1991 Physica Scripta T36, 199
- [5] Coulson D., unpublished Ph.D. Thesis, Princeton University 1994
- [6] Gradshteyn I.S. & Ryzhik I.M., *TABLES OF INTEGRALS, SERIES, AND PRODUCTS* , Academic Press 1980
- [7] Hu W., Seljak U., White M. & Zaldarriaga M. 1997, Phys.Rev.D 56, 596, astro-ph/9709066; Hu W. & White M. 1997 Phys.Rev.D 56, 596, astro-ph/9702170; Hu W. & Sugiyama N. 1995, Ap.J. 444, 489, astro-ph/9407093
- [8] Kofman L., Linde A. & Starobinsky A. 1997, Phys.Rev.D 56, 3258
- [9] La D. 1991, Phys. Lett. B 265, 232; Turner M.S., Weinberg E.J. & Widrow L.M. 1992, Phys.Rev.D 46, 2384; Occhionero F. & Amendola L. 1994, Phys. Rev. D 50, 4846
- [10] Kaiser N. & Stebbins A. 1984, Nat. 310, 391; Bouchet F., Bennet D. & Stebbins A. 1988, Nat. 355, 410
- [11] Mukhanov V.F. , Feldman H.A. & Brandenberger R.H. 1992 Phys.Rep. 215, 203
- [12] Lasenby A.N., Jones A.W. & Dabrowski Y., 1998 Phil. Trans. R. Soc. Lond. A. in press, astro-ph/9810196
- [13] Ma & Bertschinger 1995, Ap.J. 455, 7
- [14] Padmanabhan T. *Structure formation in the universe* , Cambridge University Press 1993
- [15] Planck Surveyor: <http://astro.estec.esa.nl/SA-general/Projects/Planck/> ; Microwave Anisotropy Probe: <http://map.gsfc.nasa.gov/>
- [16] Tkachev I., Khlebnikov S., Kofman L. & Linde A. 1998, Phys.Lett. B 440, 262, hep-ph/9805209
- [17] White M., Krauss L.M. & Silk J. 1993 Ap.J. 418, 535

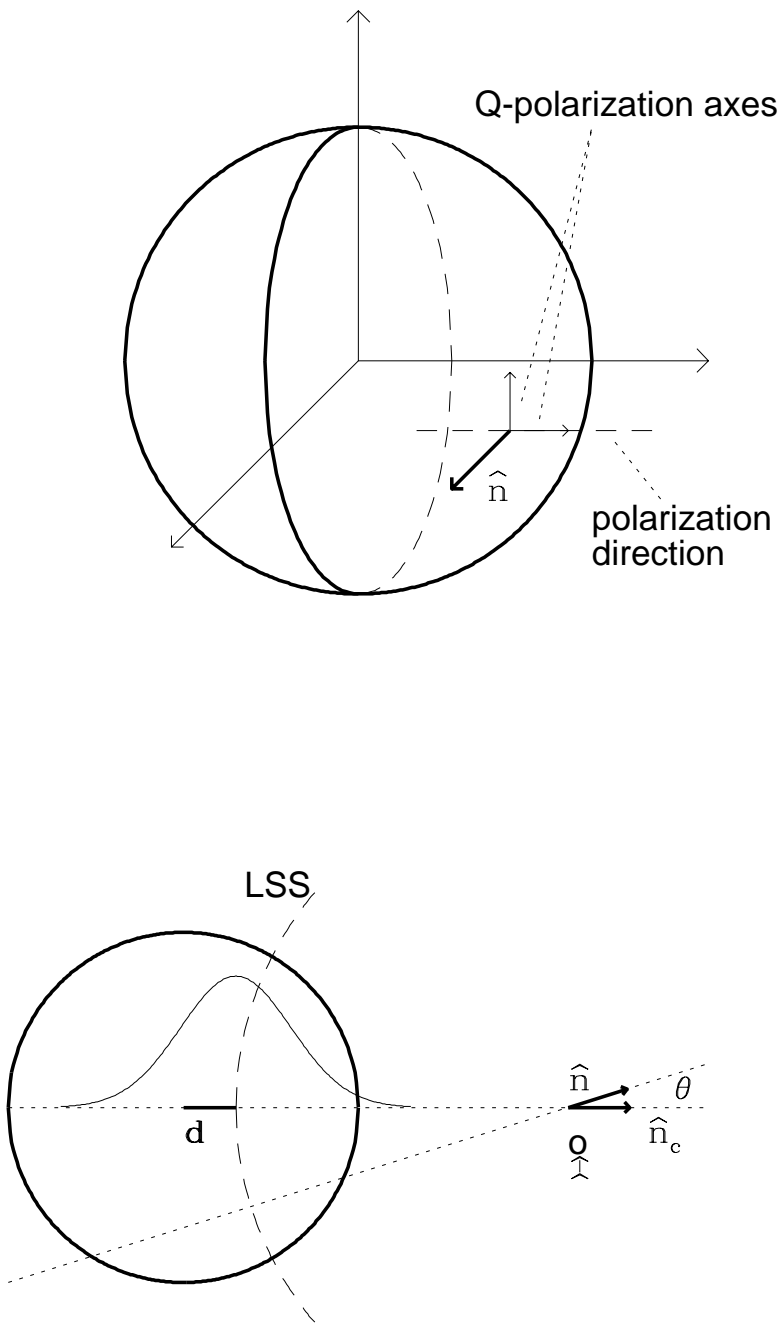


FIG. 1. Upper panel: polarization within a spherical seed. The axes displayed show the geometric directions for which the polarization is given by a Q term only, thus fixing the polarization direction as displayed. Lower panel: CMB anisotropies from a spherical seed. Its center has a distance d from the last scattering surface; the anisotropy is symmetric under rotations around \hat{n}_c and depends geometrically on the angle θ only.

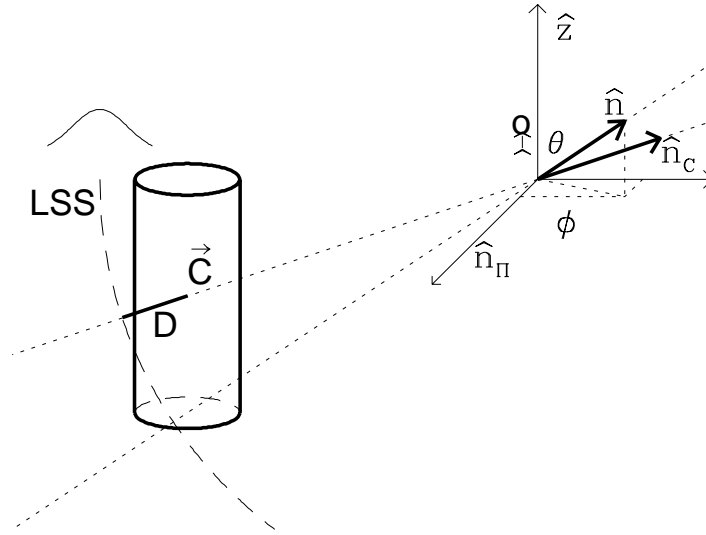
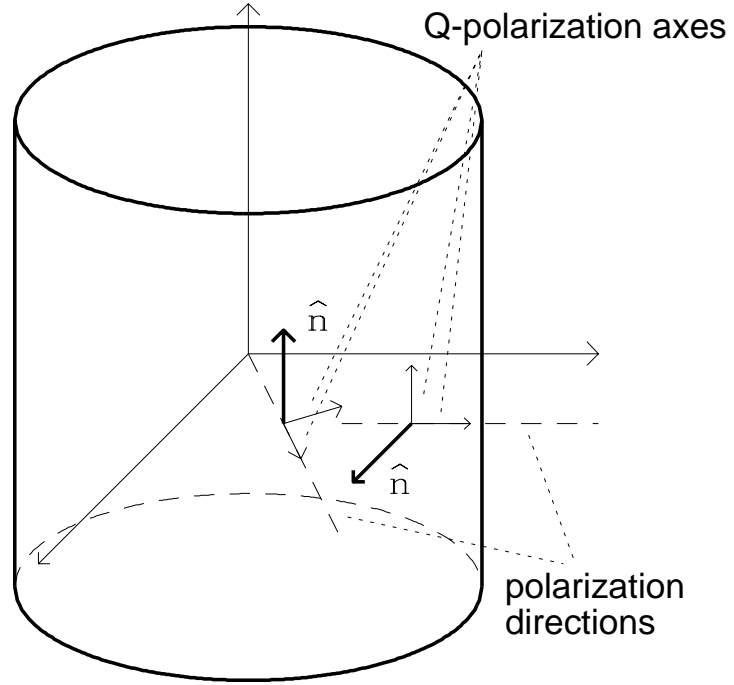


FIG. 2. Upper panel: polarization within a cylindrical seed. For the cases of propagation parallel and orthogonal to the symmetry axis, the axes displayed show the geometric directions for which the polarization is given by a Q term only, thus fixing the polarization directions as displayed. Lower panel: CMB anisotropies from a cylindrical seed: a view of the Π plane. The representative point \vec{C} has a distance D from the last scattering surface; the anisotropy is symmetric under reflections on Π and depends geometrically on the angle θ and on $|\pi/2 - \phi|$.

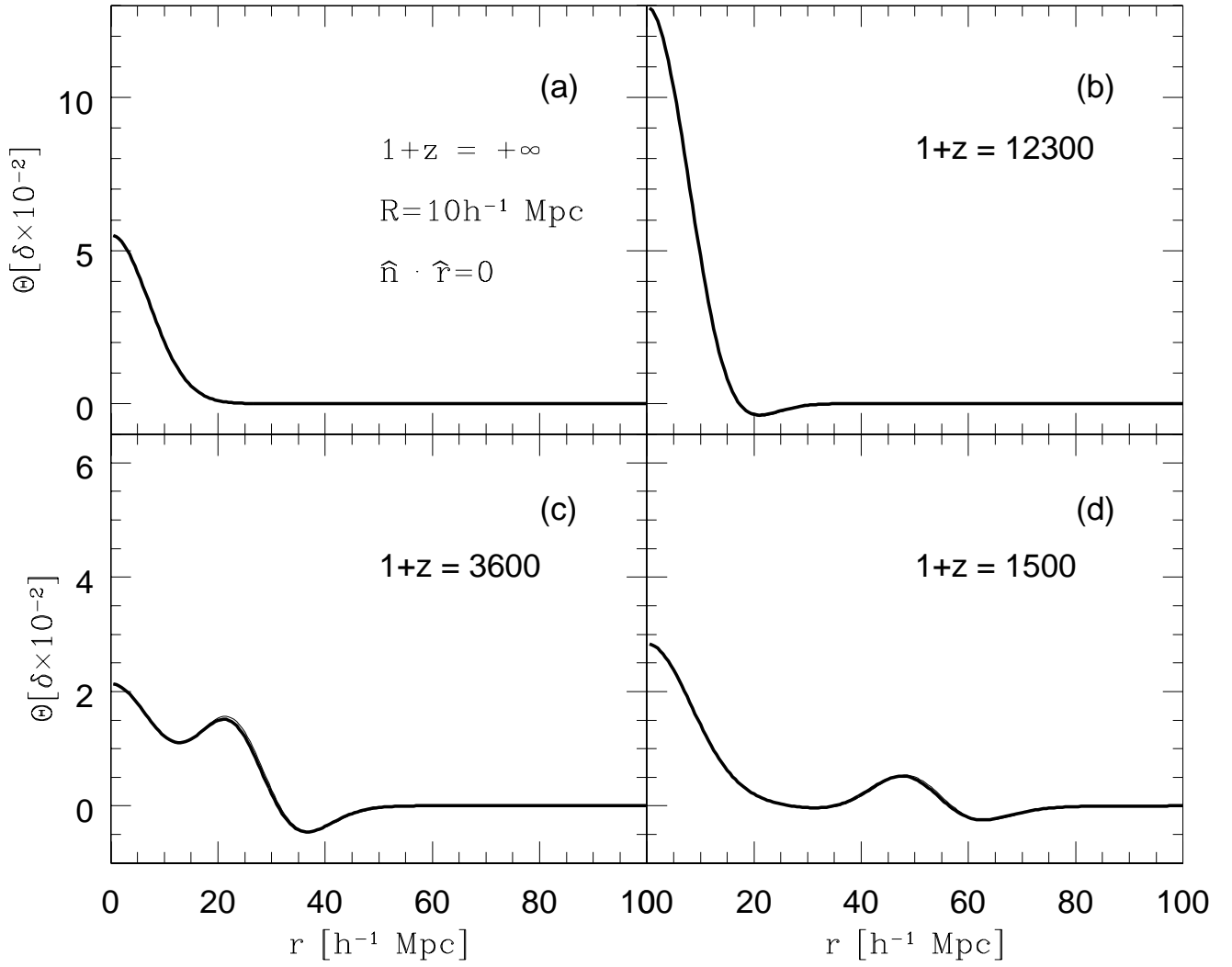


FIG. 3. CMB temperature perturbation around a spherical seed with the indicated size as a function of the radial distance from the center; the different panels represents the perturbation at different times. Note the temperature waves arising from the oscillations occurring at the horizon crossing.

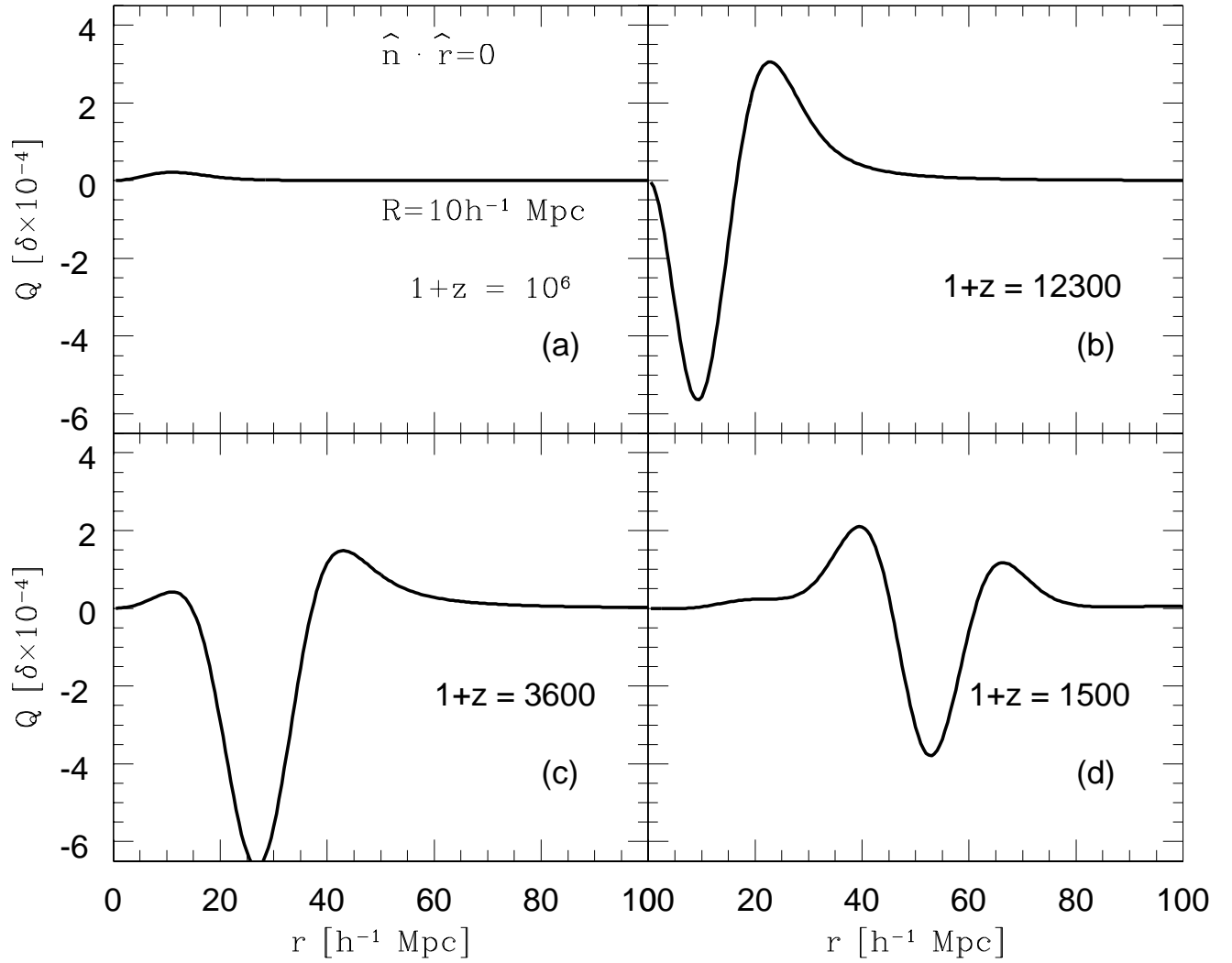


FIG. 4. The CMB polarization perturbation around a spherical seed is plotted as in figure 3. Note the external polarization waves at the position of the CMB sound horizon at the time considered and the absence of central perturbation.

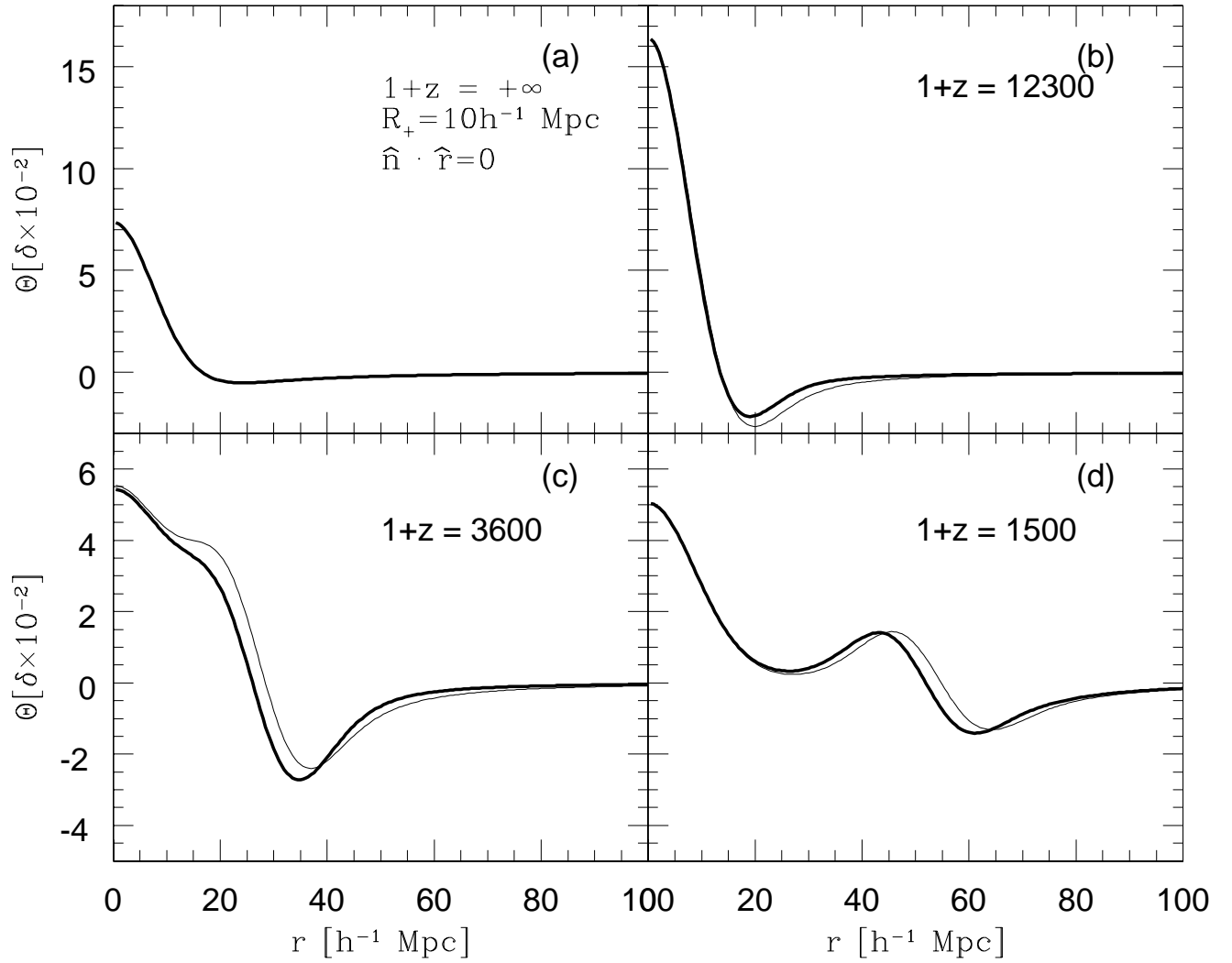


FIG. 5. CMB temperature perturbation around an infinite cylindrical seed with the indicated size on the equatorial plane, as a function of the distance from the symmetry axis. The different panels represent the perturbation at different times. Note, in analogy with the spherical case, the temperature waves arising from the oscillations occurring at the horizon crossing.

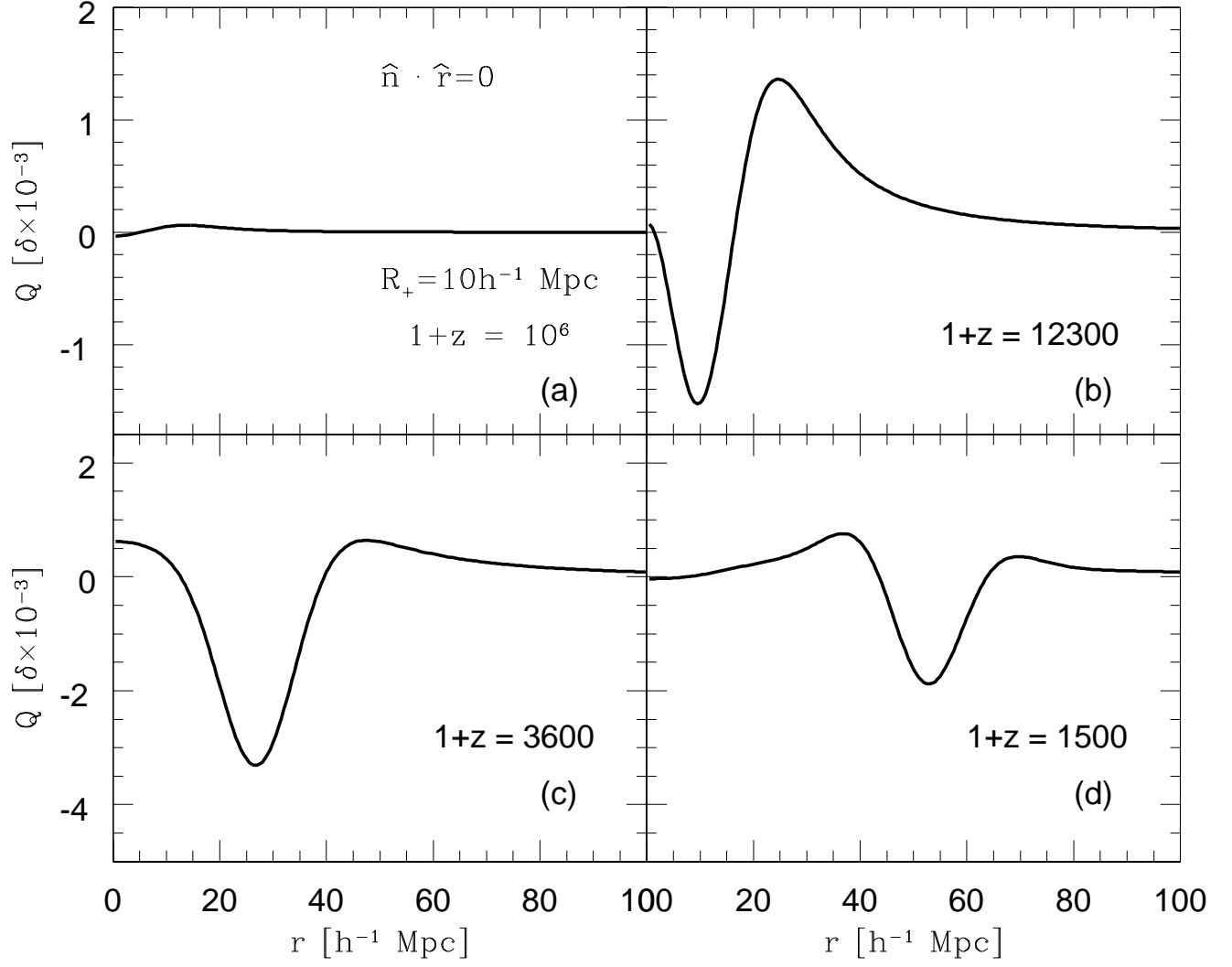


FIG. 6. The CMB polarization perturbation around a infinite cylindrical is plotted as in figure 5. In this case, since photons are propagating as indicated, a central polarization arises, mostly evident in panel *c*.

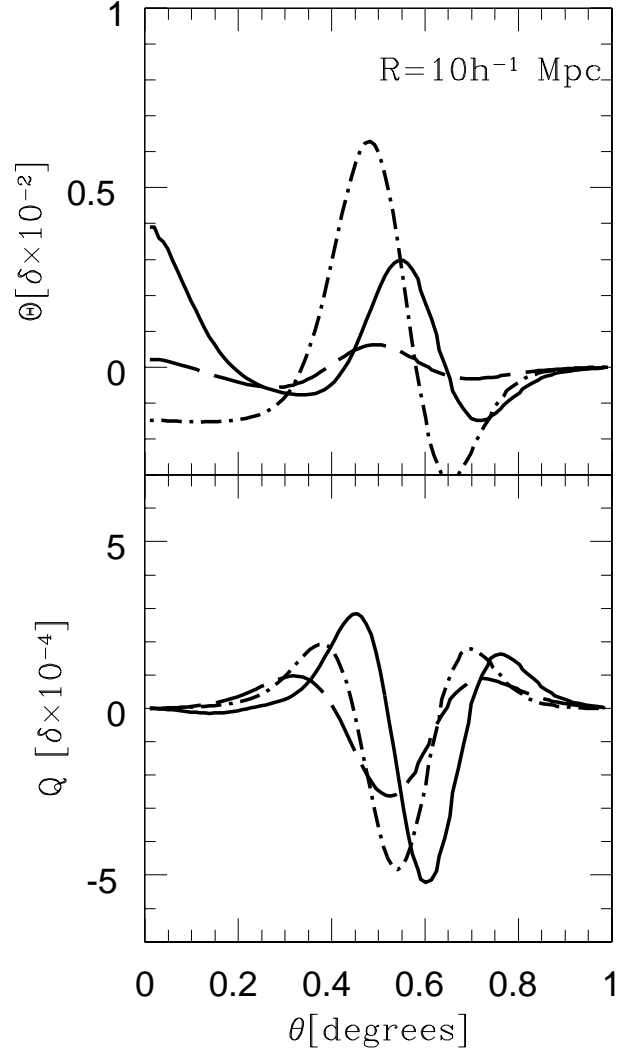


FIG. 7. CMB temperature (top) and polarization (bottom) anisotropy for a spherical seed with the size indicated; θ is the angle from the center. The seed is centered exactly on the last scattering surface ($d = 0$, solid line), just in front of it ($d = 30h^{-1}$ Mpc, dashed line), and behind ($d = -30h^{-1}$ Mpc, dotted dashed line). It physically occupies the very central part of the graph, $\theta \leq 10'$. Note the temperature and polarization anisotropy waves at the angular scale corresponding to the CMB sound horizon at decoupling.